Accepted Manuscript

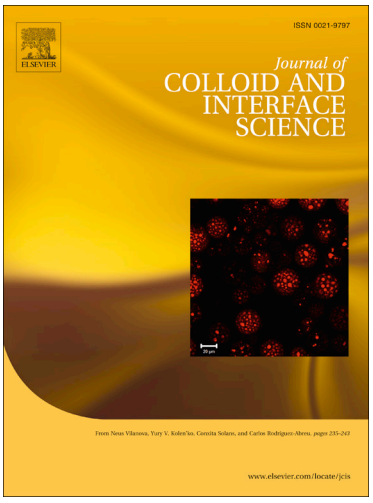

Antireflective mesoporous silica coatings by optimization of water content in acid-catalyzed sol-gel method for application in glass covers of concentrated photovoltaic modules

Cecilia Agustín-Sáenz, Maider Machado, Agnieszka Tercjak

PII: S0021-9797(18)31118-4
DOI: https://doi.org/10.1016/j.jcis.2018.09.043
Reference: YJCIS 24094

To appear in: *Journal of Colloid and Interface Science*

Received Date: 4 July 2018
Revised Date: 11 September 2018
Accepted Date: 12 September 2018

Please cite this article as: C. Agustín-Sáenz, M. Machado, A. Tercjak, Antireflective mesoporous silica coatings by optimization of water content in acid-catalyzed sol-gel method for application in glass covers of concentrated photovoltaic modules, *Journal of Colloid and Interface Science* (2018), doi: https://doi.org/10.1016/j.jcis.2018.09.043

Title: Antireflective mesoporous silica coatings by optimization of water content in acid-catalyzed sol-gel method for application in glass covers of concentrated photovoltaic modules

Authors:

Cecilia Agustín-Sáenz (a), Maider Machado (a), Agnieszka Tercjak (b)

Address:

(a) TECNALIA (Energy and Environment Division) - Parque Científico y Tecnológico de Gipuzkoa, Mikeletegi Pasealekua 2, Donostia - San Sebastián, Spain
(b) Group `Materials + Technologies´ (GMT), Department of Chemical and Environmental Engineering, Faculty of Engineering, Gipuzkoa, University of the Basque Country (UPV/EHU), Plaza Europa 1, 20018 Donostia-San Sebastián, Spain

*Corresponding autor:

Cecilia Agustín-Sáenz

https://orcid.org/0000-0003-1210-9727

Postal address: Mikeletegi Pasealekua 2, 20009 Donostia - San Sebastián, Spain.

Tel.: +34 667 115 865

e-mail address: cecilia.agustin@tecnalia.com

GRAPHICAL ABSTRACT

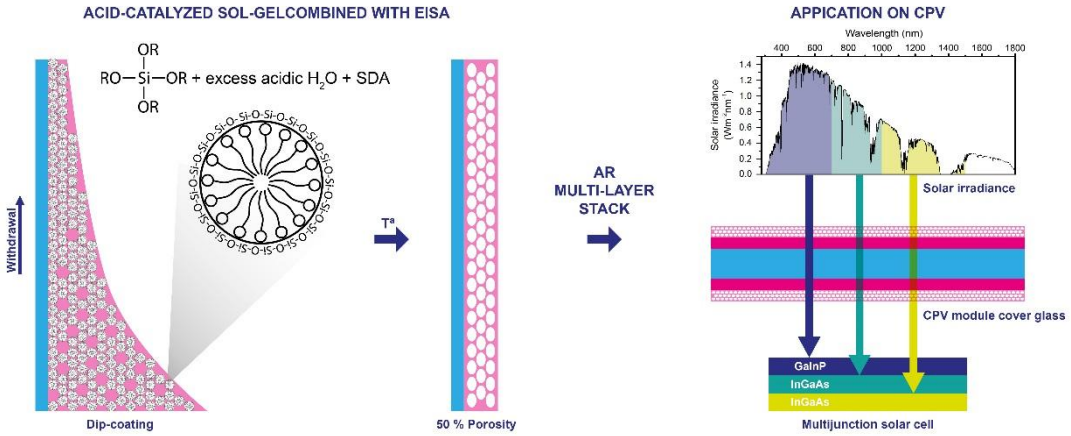

ABSTRACT

Porous silica layers with outstanding antireflective properties have been prepared by acid-catalyzed sol-gel process in presence of organic phases as structure directing agents (SDA) and excess water, with the aim of offering a cost-competitive, easy up-scaling and high efficiency process that contributes to reduce current levelized cost of energy (LCOE) of concentrating photovoltaics (CPV). The process has been optimized by controlling the water/alkoxide ratio, which is an important structure-regulating tool, having a strong influence in the structural properties of sol-gel synthesized materials. Hydrolysis of the inorganic precursor has been accomplished in high water/alkoxide conditions and in the presence of SDAs. Evaporation induced self-assembly (EISA) during coating deposition and the scanning of four types of SDAs have permitted to select the coating that fulfilled specific thickness and refractive index values with, in parallel, excellent results on sol stability. The final optimization has produced mesoporous coatings with ~ 9 nm mean pore size, leading to an enhancement in transmittance up to 7.4 % over bare glass in the 300 to 1500 nm wavelength range. The transmittance spectra have been used as inputs for the theoretical calculation of the short-circuit current density of a commercially available multijunction solar cell for

CPV applications.

KEYWORDS: Antireflection; silica; porous coating; acid-catalyzed; sol-gel

Abbreviations: AFM, atomic force microscopy; AR, antireflective; BEMA, Bruggeman effective medium approximation; CPV, concentration photovoltaic; DNI, direct normal irradiance; EEP, environmental ellipsometric porosimetry; EISA, evaporation induced self-assembly; EQE, external quantum efficiency; LCOE, levelized cost of energy; NMR, nuclear magnetic resonance; PV, photovoltaic; RH, relative humidity; SDA, structure directing agent; TEOS, tetraethyl ortho silicate; TGA, thermogravimetric analysis; WCA, water contact angle.

1. INTRODUCTION

Concentrated photovoltaic (CPV) technology is currently considered as a utility-scale option for clean, renewable energy generation [1]. It is based on expensive but high efficient multijunction III-V solar cells whose conversion efficiency can currently yield up to ~ 46% at cell level and 38.9 % at module level [2][3]. Additionally, refractive or reflective cost-effective optical elements permit to operate at light concentration levels up to 1000X and thereby reduce cell area. In high direct irradiation conditions, this technology has the potential to provide electricity at competitive costs. Current levelized cost of energy (LCOE) for large scale CPV ranges from 0.10 €/kWh to 0.15 €/kWh for locations with direct normal irradiance (DNI) of 2000 kWh/m^{2}a and 0.08 €/kWh to 0.12 €/kWh for 2500 kWh/m^{2}a DNI [1]. According to the SunShot Initiative, LCOE should reach a cost of 0.03 $/kWh for utility-scale, 0.04 $/kWh for commercial, and 0.05 $/kWh for residential systems by 2030 [4] [5]. One of the possibilities to reduce LCOE for CPV technology is to improve the optical performance at module level.

Photovoltaic components (cells, connections, etc.) need protection from the harsh environmental conditions to which they are exposed during their service life. This function is usually provided by low iron float glass [6]. Glass transmission properties

can be enhanced by antireflective (AR) coatings [7] which, in order to effectively contribute to LCOE reduction, should be deposited by means of a cost-competitive, easy up-scaling and highly efficient process.

In a previous work [8], broadband antireflective behavior of multi-layer stacks was discussed and an acid-catalyzed sol-gel approach was conducted in order to obtain AR silica coatings with controlled thickness and refractive index values, provided by the setting of synthesis parameters such as the ratio of inorganic and organic phases and their concentration. In this approach, coating mesostructure during deposition is led by the creation of micelles formed by the organic phases that serve as a template for the inorganic network growth, as first evidenced through Evaporation Induced Self-Assembly (EISA) method by Asefa et al. [9] and Brinker et al. [10]. The mesoporous structure is obtained after calcination of the organic phase. Regarding the inorganic network, acid-catalyzed synthesis, unlike the base-catalyzed one, leads to the formation of a material with an extended linear or randomly branched structure, with the advantage of obtaining coatings with robust mechanical properties and good adhesion, as well as sols with long-term stability [11]. Base-catalyzed synthesis leads to formation of highly crosslinked discrete polymeric clusters that promote a porous structure with poorer mechanical properties and more instable sols, whereas colloidal suspensions are formed by highly crosslinked dense particles that may also be built by base-catalysis [12].

By adjustment and selection of the synthesis parameters and organic phases as structure directing agents (SDA), acid-catalyzed sol-gel approach results in a proper method to control the microstructure, the pore volume and pore size of the coating, while obtaining highly stable sols and materials. Firstly [8], tetraethyl ortho silicate (TEOS) was hydrolyzed with four equivalents of acidified water in the presence of ethanol as

homogenizing agent and four organic SDAs, that were scanned as templates. Based on the extensive range of possibilities that this technique offers, the present work accomplishes a consistently improved approach in which eight equivalents of acidified water to hydrolyze TEOS in the presence of ethanol have been added instead of four. The structural properties of the sol-gel prepared materials are strongly affected by the process parameters and, particularly, by the water/alkoxide molar ratio (R_w), which is an important structure-regulating tool [13].

In acid-catalyzed approach, low R_w conditions lead to the beginning of the condensation of siloxane bonds prior to the completion of the hydrolysis. This condensation takes place on terminal silanols, thus leading to the formation of weakly branched chain-like networks. High R_w conditions (>> 4) foster a hydrolysis step which can be fully completed before condensation [14], which, in turn, is favored through the water producing reaction rather than the alcohol producing one, according to Fig. 1. The water produced by condensation causes a complete hydrolysis and enhances the depolymerization rate that occurs preferentially at less stable sites [11]. Subsequent repolymerization forms stable configurations at the expense of unstable ones, which finally leads to the increase of branching in chains whose structure may be closer to that of discrete colloidal particles from base-catalysis. Particularly, the formation of uniform-size colloidal silica from base-catalyzed TEOS was first reported by Stöber et al. [15], who obtained spherical particles sized from a few nanometers to almost a micron for crescent catalyst concentrations. The silicate condensation sequences from atomic or molecular scale (monomer, dimer, linear or cyclic trimer, cyclic tetramer, and higher order generation of discrete colloidal particles) obtained from acid-catalyzed TEOS has been investigated by Engelhardt et al. [16] by ^{29}Si Nuclear Magnetic Resonance. By further connection of the single rings and chains, two-dimensional single

layers shall be first formed that subsequently will lead to three-dimensional frameworks [17]. The coatings processed with such acid-catalyzed TEOS in high R_w conditions will result in a more branched network with respect to the low R_w cases, thus providing higher porosity structures closer to base-catalyzed processing but simultaneously maintaining a strong adherence and good mechanical properties associated to the acid-catalyzed process. Based upon this theoretical background, some works as, e.g., Collina et at. [18] demonstrated that the surface area of acid-catalyzed TEOS porous gels strongly increased for R_w values raising up to ten.

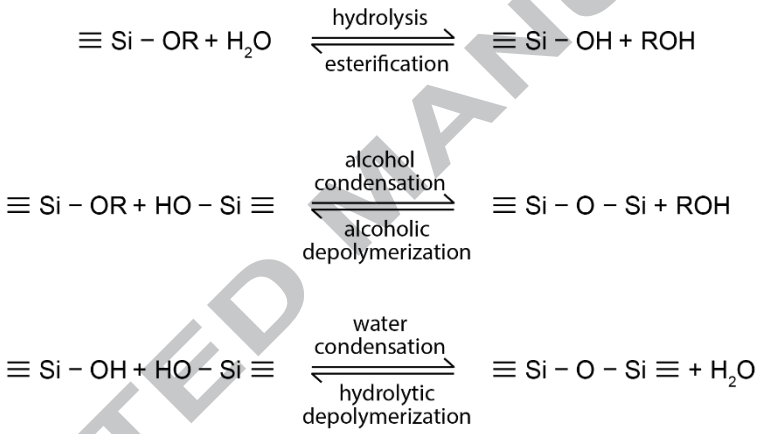

Fig. 1. Hydrolysis, condensation and reversed reactions of Si alkoxide.

Some works have reported acid-hydrolyzation of TEOS for the preparation of AR coatings using a R_w 2 stoichiometric ratio of acidified water [19–21], other studies use R_w between 3 – 5 [22–25], while only Y. Xu et al.[26] and R. Prado et al. [27] prepared silica sols by hydrolyzing TEOS in high R_w conditions of 12 and 16, respectively. They obtained coatings with good antireflective performance, although they did not focus on aging and durability of the prepared sols.

The aim of this work is to further improve the efficient approach for the deposition of highly performing AR multi-layer stacks in CPV applications presented in a previous

article [8], additionally considering the environmental-friendliness, cost-effectiveness and easy up-scaling characteristics of the process, also providing a good sol stability and durability of the coatings. The theoretical calculation of the optical properties of multilayer coatings presented in [8] allowed to design and select the stack that better matched the spectral response of multijunction solar cells, considering that outstanding stability of the antireflection properties was also required [8]. The target was to develop a bi-layer stack composed by a 106 nm thickness and 1.41 refractive index at 700 nm inner layer and a 119 nm thick, 1.22 refractive index at 700 nm -tailored by porosity control- outer layer. Although a significantly enhanced antireflective performance was shown, further optimization is proposed herein through the preparation of acid-catalyzed sol-gel formulations with higher R_w. Coatings with increased porosity (50 % versus 45%) have led to an additional enhancement of the transmittance of the cover glass. The advantages of the acid-catalyzed approach, such as long stability of the sols and more robust mechanical properties of the derived coatings, have been added to the system. The effect of the coatings on the short-circuit current density of a simplified CPV mono-module device has been calculated and quantified for the external quantum efficiency (EQE) and reflectance spectra of a commercially available multijunction solar cell.

2. MATERIALS AND METHODS

2.1. Materials.

Absolute ethanol (99.9 % purity) and tetraethyl orthosilicate precursor (TEOS, 98 % purity) were purchased from Scharlau and Acros respectively, and used as received. Catalyst hydrochloric acid (HCl, 37 % vol) was purchased from Scharlau and was used to prepare a 0.1 M solution in distilled water. Organic structure directing agents (SDA) were polyethylene glycol hexadecyl ether di-block copolymer -of an average molecular

weight ~ 1124 g/mol- (SDA1); cationic cetyltrimethylammonium bromide -with 364.45 g/mol molecular weight- (SDA2); poly(ethylene oxide)-b-poly(propylene oxide)-b-poly(ethylene oxide) tri-block copolymer -of an average molecular weight ~ 12600 g/mol- (SDA3) and t-octylphenoxypolyethoxyethanol di-block copolymer -of an average molecular weight ~ 625 g/mol- (SDA4) . All of them were purchased from Sigma-Aldrich and used as received.

Optiwhite® 4 mm low iron soda lime float glass from Pilkington was used as substrate.

2.2. Preparation of sols.

Silica sols were prepared via acid catalysis following a two-step procedure. In a first step, TEOS, ethanol, acidified water (0.1 M HCl) and 4 different SDAs with concentration values from 25 to 150 g/L were mixed and stirred for 90 min at 60 ºC. In a second step, a mixture of ethanol and acidified water (up to R_w 8) was added drop by drop to the solution and was stirred for 60 min at 40 ºC. Sols with no SDA content were also prepared with R_w 4 and R_w 8. The resultant sols were aged in sealed glass containers for 2 days. Different equivalent concentrations of SiO_2 were prepared by varying ethanol/TEOS ratio (R_{Et}). Sols with R_{Et} 4 were prepared only for NMR study, sols with R_{Et} 8.7 were denoted as H-sols and those with R_{Et} between 22 – 25 were denoted as L-sols.

2.3.Preparation of mono-layers.

Silica sols were deposited on 4 mm (thick) low iron float glass specimens after being cleaned in ethanol under sonication for 15 min and then air dried. The coating deposition was performed on both sides of the low iron float glass by dip coating at a

controlled withdrawal rate of 5 cm/min. After coating deposition, a sintering step was performed in a conventional furnace between 350 - 550 ºC in air atmosphere for 1 h.

2.4. Characterization.

The kinematic viscosity of the sols was measured at 22 ºC by means of Ubbelohde viscometer, through which the liquid flows through a capillary tube due to gravity. Different types of capillary tubes were used depending on viscosity values. Type 0B was used for sols with kinematic viscosity between 1-5 cSt and type 1C was used for sols with kinematic viscosity between 6-30 cSt. Dynamic viscosity (μ) was obtained by multiplying the kinematic viscosity by the density values previously determined with a pycnometer/specific gravity bottle. The stability of final liquid sols, which is related to pot life, was characterized by viscosity measurements along six months after preparation. Viscosity increase was calculated as the percentage of the increment of viscosity after certain aging time over the initial value presented by each sol [$(\mu_{aging}-\mu_{initial})/\mu_{initial}\cdot 100$].

^{29}Si nuclear magnetic resonance (NMR) spectra were obtained at room temperature on a Bruker AVANCE III 500 spectrometer equipped with an 11.7 T magnet (99.36 MHz for ^{29}Si). After preparation, the sol was placed in NMR tubes (5 mm of diameter) adding 50 μl of deuterated methanol and 50 μl of trimethyl silane and inserted into the magnet. The experiment was accomplished using a single 60 degrees pulse. The number of data points was 16 K, with a 300 ppm bandwidth, 1024 scans and 5 s relaxation delay. Spectra were processed using a20 Hz exponential apodization function and the ^{29}Si NMR background signal from the NMR probe and tube was subtracted.

Ellipsometric parameters ψ and Δ, which are functions of the complex refractive index ($\tilde{n} = n + ik$), were recorded by a variable angle spectroscopic ellipsometer (M-

2000UTM, J.A. Co., Woollam). Spectra were recorded from 250 to 1000 nm at three incidence angles between 60 – 75 º. The spectra were fitted using both the Cauchy dispersion model [28] and Bruggeman medium effective approximation model [29]. The fitting allowed the calculation of relevant parameters such as refractive index, *n*, extinction coefficient, *k*, coating thickness, *d*, and porosity. The apparent porosity was calculated with respect to pure dense silica and a polarization factor of 0.33 was considered. The data analysis was performed with WVase32 software.

Water adsorption-desorption processes were studied by environmental ellipsometric porosimetry (EEP) [30] [31]. The measurements were performed with the above described equipment (M-2000UTM, J.A. Co., Woollam), within a cell with controlled relative humidity (RH). In this case, the spectra were taken at a fixed incident angle of 70 º, at different RH values. Using the Cauchy fitting model, *n* values were obtained as a function of RH. The absorption-desorption isotherms were calculated using Bruggeman medium effective approximation fitting, using the optical characteristics of the dense part of the porous media. Pore size distribution was determined using modified Kelvin's equation, which takes into account Tolman correction and pore anisotropy as proposed by Boissiere et al. [30].

The surface morphology of the investigated coatings was analyzed using atomic force microscopy (AFM). AFM phase and height images were collected by operating in tapping mode with a scanning probe Multimode 8 microscope from Bruker with Nanoscope V controller. The AFM was equipped with an integrated silicon tip/cantilever having a resonance frequency of ~300 kHz and a 42 N m^{-1} spring constant. Scan rates ranged from 0.7 to 1.2 Hz s^{-1}. In order to get repeatable results, different regions of the investigated coatings were scanned to choose representative AFM images.

Water contact angle (WCA) was determined by the static drop method, using Digidrop Contact Angle Meter (GBX Instruments). Ten measurements were taken on each sample to provide mean and standard deviation values.

Thermogravimetric analysis (TGA) was accomplished in TG-DTA92 thermobalance. Organic SDA were subjected to a measurement program from 25 ºC up to 1000 ºC at 5 ºC/min heating rate in air. The analyzed sols were subjected to a measurement program from 25 ºC up to 350 ºC at 5 ºC/min heating rate, dwelled for 60 min at 350 ºC, and raised up to 1000 ºC at 10 ºC/min heating rate in air.

Transmittance and reflectance spectra of the investigated AR coating stacks were measured with a Jasco V-670 UV-Vis-NIR spectrophotometer, equipped with a 150 mm integrating sphere. Spectra were taken in the 300 to 2000 nm wavelength range. Integrated transmittance, τ, was calculated by weighting transmittance values with AM1.5 solar spectral irradiance [32] according to Equation 1.

$$\tau = \frac{\int_{\lambda_1}^{\lambda_2} T_1(\lambda) \cdot \varphi_{AM1.5}(\lambda) \mathrm{d}\lambda}{\int_{\lambda_1}^{\lambda_2} \varphi_{AM1.5}(\lambda) \mathrm{d}\lambda} \qquad \text{Equation 1}$$

where T_1 is the transmittance spectrum of the coated glass, $\varphi_{AM1.5}(\lambda)$ is the AM1.5 solar spectrum [32] and λ_1 and λ_2 define the wavelength range in which τ is calculated. Integrated reflectance, ρ, was obtained in a similar way using the measured reflectance spectrum. Gain value was calculated as the percentage of the increment of τ value of coated glass over bare glass $[(\tau_{coat}-\tau_{glass})/\tau_{glass} \cdot 100]$.

The effect of the developed coatings on the electric performance of multijunction photovoltaic cells for CPV applications was quantified through the calculation of the short-circuit current density (J_{sc}) of a simplified (cover glass + cell) device, by using

Equation 2.

$$J_{sc} = q \int_{\lambda_1}^{\lambda_2} \phi(\lambda) EQE(\lambda) d\lambda, \qquad \text{Equation 2}$$

where q is the elementary electric charge, $\phi(\lambda)$ is the incoming photon flux, $EQE(\lambda)$ is the external quantum efficiency of the cell and λ_1 and λ_2 define the wavelength range where J_{sc} is calculated.

The calculation of the incoming flux considered the coupled effect of glass transmittance and cell reflectance through Equation 3, derived from standard net radiation methods [3] [33].

$$\phi(\lambda) = \varphi_{AM1.5}(\lambda) \frac{T_1(\lambda)}{1 - R_{12}(\lambda) R_{21}(\lambda)} \qquad \text{Equation 3}$$

where $\varphi_{AM1.5}$ is the AM1.5 solar spectrum [32], T_1 is the transmittance of the coated glass, R_{12} is the internal air-coated glass interface reflectance and $R_{21}$is the air-cell reflectance.

EQE and reflectance curves from inverted metamorphic tri-junction solar cell (IMM3J) were taken for the calculation [34][35][36] and are depicted in Fig. 2. This cell has demonstrated an efficiency of 40.8 % at 326 suns [37]. The integration interval was calculated independently for top, middle and bottom subcells.

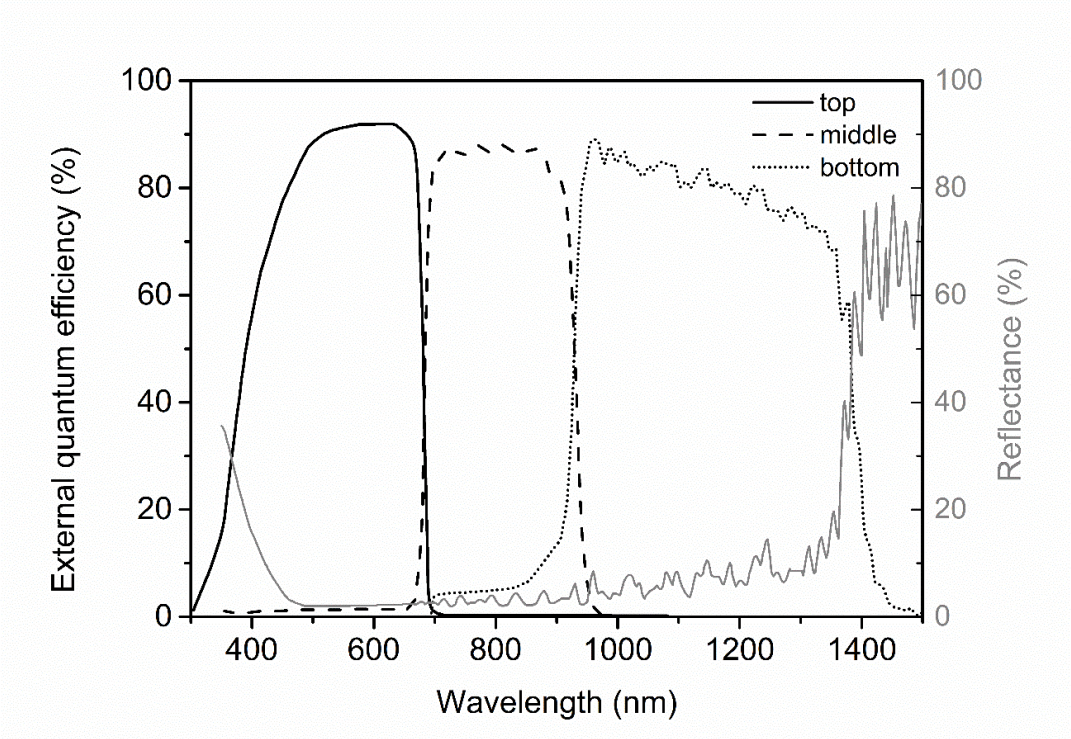

Fig. 2. External quantum efficiency (%) and reflectance (%) of IMM3J cell.

3. RESULTS AND DISCUSSION

3.1.Effect of R_w and organic SDA type in sol-gel transition.

The sol-gel transition in tetra alkoxides-based systems such as TEOS is characterized by a strong increase in sol viscosity [38]. The time evolution of this parameter was registered, due to the direct influence it has in the pot life of sols. The viscosity changes according to the formation and the growth of the polymer-like silica, that may be linear chains, ring-like chains or form branching and interconnected chains, until the formation of the gel structure is reached. Preparing high stable sols is of interest for CPV applications since it permits to obtain an efficient, robust and scalable process for AR coating deposition. The viscosity of H-sols periodically registered along one-year period without SDA prepared with R_w 4 and 8 at different aging times is presented in Fig. 3a.

Under acid-catalysis, the role of excess water above four equivalents, R_w 4, on gelation time depends also on the experimental conditions such as pH and alcohol content [39]. Several postulations have been both theoretically and experimentally studied in terms of a high R_w formulated sol. It has been shown that a high R_w may shorten gelation time. However, it has also been stated that a minimum gelation time close to R_w 4 may be obtained. Depending on the structures that are promoted or inhibited under each particular synthesis, the size of the sol particles changes continuously during the nucleation and growth process [38], due to the direct and the reverse reactions explained in Fig. 1. For example, if ring-like structure formation is inhibited by some process, it may provoke also a retardation of gelation [39]. Therefore, it is crucial to analyze the viscosity evolution of each investigated system.

Regarding the systems under study, the initial viscosity of the sol with four water equivalents was 2 mPa·s, while the formulation with excess water exhibited 2.6 mPa·s. As observed in Fig. 3a, both synthesis routes showed a similar evolution of viscosity along a one-year duration, and they exhibited an increase of around 18 % and 24 %, respectively, after 6 months of aging. Moreover, both doubled the initial value of viscosity after one year. This was an outstanding result from the point of view of sol durability. This evolution showed independence from R_w in this system, since the viscosity evolution of the two sols suffered a parallel increase.

Concerning the silanol and condensed silica species in the sols, Pouxviel et al. [14], who studied the sol-gel polymerization of TEOS with four water equivalents, R_w 4 and R_w 10 by ^{29}Si NMR in the early stages after preparation, observed that silanol and condensed species were the same in both cases and only differences in peak intensities were found. However, they stablished that only with high R_w hydrolysis and condensations reactions were totally separated, based on the fact that the concentration of Si-OR species

disappeared rapidly. In Fig. 4, the ^{29}Si NMR performed after 2 days did not show silanol groups (peaks around – 80 ppm) in none of the sols. The silica oligomers for R_w 4 (Fig. 4a) were mainly formed by condensed linear or ring-like chains and branched silica species, thus Q_2 and Q_3 respectively (localized between – 90 ppm and – 106 ppm) after 2 days. Totally branched silica, Q_4 species (around -110 ppm) were detected after 7 and 15 days of aging whereas after 35 days only Q_3 species composed the sol. Therefore, in this case, depolymerization and subsequent repolymerization seemed not to reach equilibrium. However, the silica oligomers for R_w 8 (Fig. 4b) were linear or ring-like, Q_2 species, and branched silica, Q_3 species, at all scanned times, thus arriving at an equilibrium in the species formed during depolymerization and subsequent repolymerization along time.

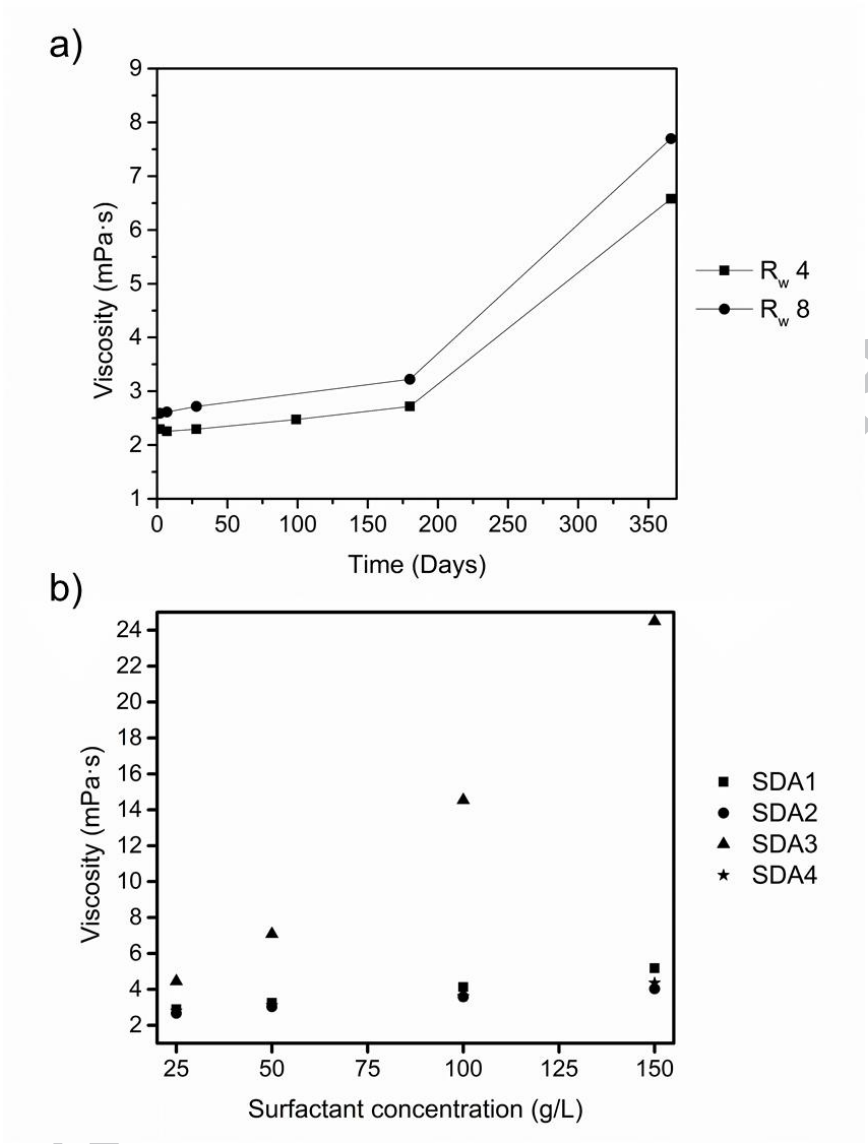

Fig. 3. The dynamic viscosity as a function of time for H-sols prepared with R_w 4 and R_w 8 (a) and effect of SDA concentration on initial dynamic viscosity of H-sols (b). (Standard deviation < 0.05 mPa·s).

Viscosity of H-sols was also measured as a function of SDA concentration for R_w 8 following the procedure described for R_w 4 in our previous work [8]. Results are drawn in Fig. 3b. The viscosity of the sols prepared with R_w 8 was in all cases slightly higher than the viscosity corresponding to R_w 4 [8]. The viscosity of the sols containing organic phases increased in the same way as for R_w 4 as long as their concentration did. Viscosity of H-sols based on SDA1, SDA2 and SDA4 started from 2.8 ± 0.1 mPa·s for

25 g/L of SDA concentration and reached 4.0, 4.4 and 5.2 ± 0.3 mPa·s for 150 g/L of SDA2, SDA4 and SDA1, respectively. The viscosity of H-sols with SDA3 varied from 4.5 to 24.5 mPa·s for the same increasing SDA concentration. The evolution of the viscosity of H-sols containing SDAs was monitored up to six months of aging. The most relevant result was that the increase of viscosity for all SDA1-sols, all SDA4-sols and SDA2-sols of 50 and 100 g /L was less than the one experimented by the sol without SDA. Therefore, the presence of organic phases contributed to improve the viscosity stability of sols. On the other hand, the 25 g/L SDA2-sol experimented an increase close to 50 %, while SDA2-sol of 150 g/L was not stable for longer than 2 days. Viscosity of SDA3-sols was measured up to one month since they experimented a two-phase separation.

The silica oligomers were also determined by ^{29}Si NMR after 2, 7 and 35 days in sols prepared with R_w 4, R_w 8 and 50 g/L of SDA1, given that the degree of condensation of inorganic chains has a crucial influence in the accommodation with organic SDA micellar phases [40]. In view of these results, shown in Fig. 4c and 4d, equilibrium states of linear or ring-like chains Q_2 and branched Q_3 silica species were detected at all times for both R_w tested, revealing an equilibrium between formed species along time in both conditions of R_w. These condensed species are excellent to accommodate around the template formed by organic micelles.

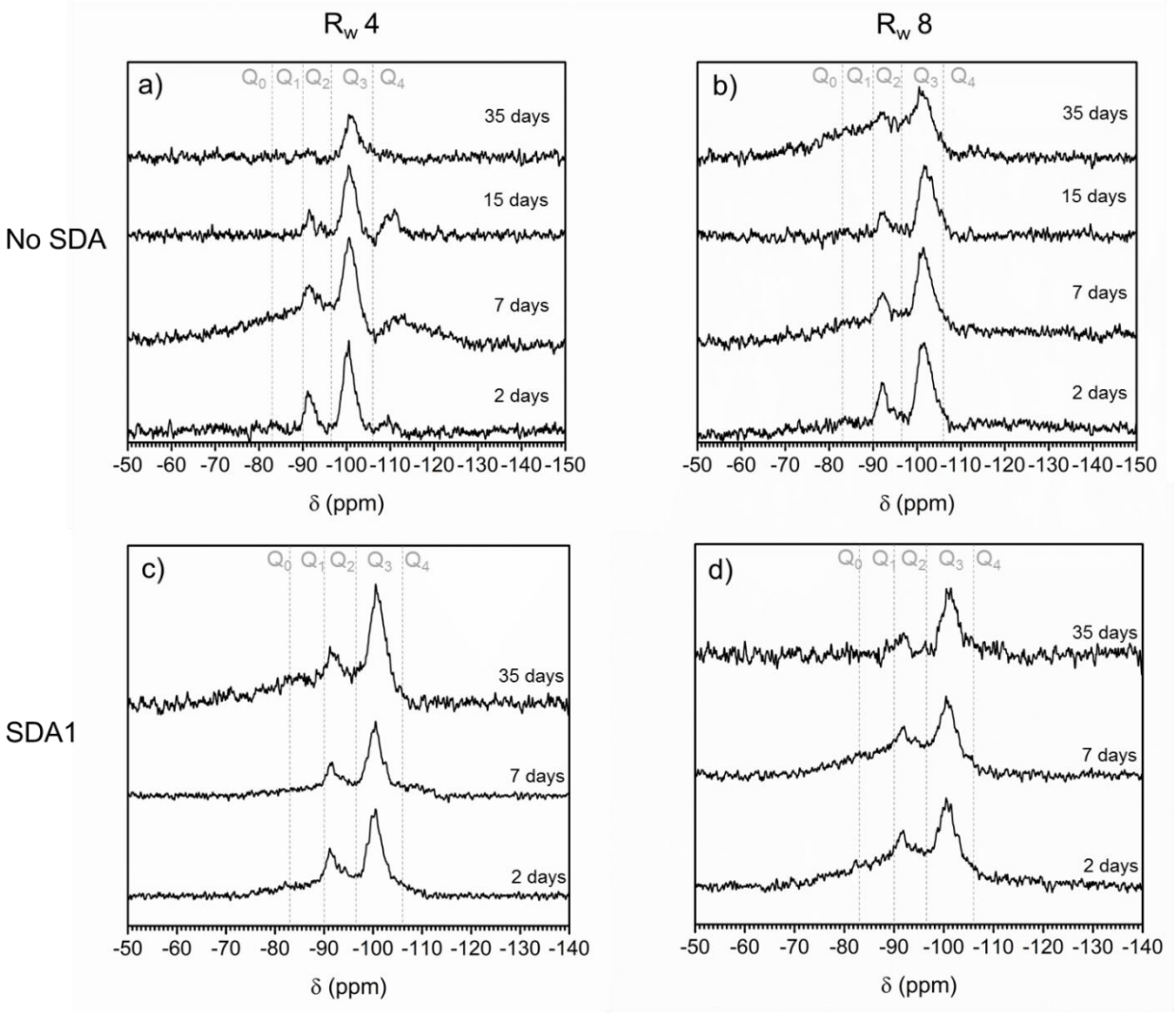

Fig. 4. ^{29}Si NMR studies of the sols prepared with R_w 4 with no SDA (a); R_w 8 with no SDA; R_w 4 with SDA1 (c); R_w 8 with SDA1 (d) measured at several times after preparation.

3.2.Effect of SDA concentration on thickness and refractive index of coatings.

The coatings grown with H-sols containing different weight concentration of the four different SDAs used in this study were analyzed by ellipsometry. The four types of organic/inorganic systems were scanned in order to obtain coatings with 50 % of void fraction and thickness around 120 nm. Thickness and refractive index obtained by ellipsometric data and fitted by Cauchy model are represented in Fig. 5a and Fig. 5b,

respectively. The apparent porosity resulting from Bruggeman fitting is graphed in Fig. 5c. The coating obtained from 150 g/L SDA2-sol was not homogeneous and transparent, therefore it was not possible to fit the ellipsometric parameters in this case.

Coating thickness increased as a function of SDA concentration as predicted by viscosity measurements. Coatings without SDA presented a 129 nm thickness. The thickness of the coatings based on SDA1- and SDA4-sols expanded from around 170 nm for 25 g/L SDA concentration to around 300 nm for 150 g/L SDA concentration. Additionally, the thickness of the coatings based on SDA3-sols expanded from around 200 nm to almost 1000 nm, for the same increasing SDA concentration. An exception was found for coatings based on SDA2, since they did not present the expected thickness increase. Regarding the nature of the organic templates, while SDA2 is a low weight cationic surfactant, SDA1, SDA3 and SDA4 are block copolymers. Therefore, since the weight concentration was the same in all the formulations, the molar ratio SDA/TEOS became different. In the case of SDA2, it seemed like the molar ratio needed to obtain the highest coating expansion was around the lower concentrations used in the preparation of these sol formulations. According to the surfactant-ethanol-water phase diagram, several nanocomposite architectures [10] [40] can be achieved thanks to a successful combination of sol-gel and self-assembly approaches. Each of the obtained micelle architecture, such as lamellar, cubic or hexagonal shall present different packing density and therefore a different film expansion. Some works [41] have compared the self-assembly characteristics of block copolymers and the low weight cationic surfactants, and several differences have been established such as the use of block copolymers allowing to obtain more complex multiscale mesostructures, thicker pore walls and adjustable pore size.

In comparison to similar coatings synthesized with R_w 4 [8], thickness values were similar for the corresponding SDA concentration. Despite the viscosity values of R_w 8-sols were higher that with R_w 4, this difference did not become detectable in terms of derived coating thickness.

H-sols with SDA1, SDA4 and SDA3 formed coatings with decreasing refractive index, with the exception of the coatings obtained with 100 g/L SDA1 and 50 g/L SDA4, that exhibited higher than expected values for such SDA concentration. The initial differences for low concentration SDA values were reduced as the concentration increased and the refractive index converged towards 1.23 similar value, with porosity being close to 50 % for the maximum SDA concentration. For all concentration values tested, only coatings derived from SDA3-sols and R_w 8 exhibited a slight increase of porosity with respect to the results corresponding to synthesis at R_w 4.

Consistently with the obtained thickness values, coatings grown with the SDA2-sols showed the lowest refractive index values at lower concentration levels in comparison to other SDAs. However, they reached their minimum value at 50 g/L SDA concentration, while the sols with higher concentration did not form porous or homogeneous coatings.

It should be noted that the use of these coatings in AR multi-layer stacks requires that specific pairs of thickness and porosity values must be jointly achieved by finding the conditions of sol preparation, given that the increase of porosity with SDA concentration was found to lead to thickness values outside the required range.

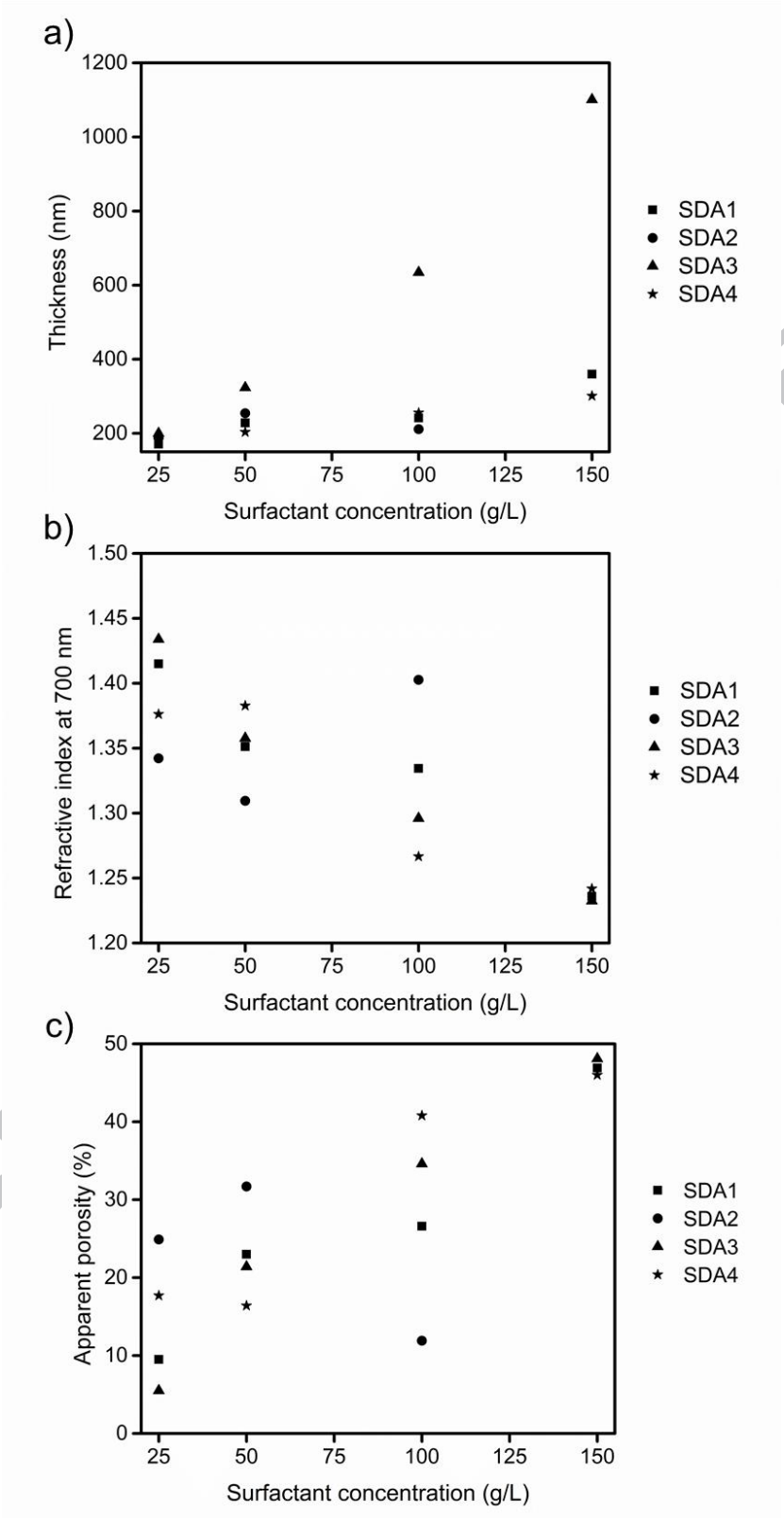

Fig. 5. Effect of SDA concentration on thickness (a) refractive index (b) apparent and porosity (c) of coatings obtained from H-sols. (d ± 0.5 nm; n ± 0.001; apparent porosity ± 0.2 %).

3.3. Effect of inorganic precursor and SDA concentration on thickness, refractive index and thermal shrinkage of coatings.

In order to obtain coatings with proper porosity-thickness tandem values to prepare highly performing AR coatings, SiO_2 concentration in the sols was adjusted. H-sols prepared with 100 and 150 g/L of SDA were mixed with ethanol in an equal volume ratio to obtain L-sols. The viscosity of sols remained stable at least after 6 months since its preparation. The optical properties of the coatings prepared with these sols were characterized by ellipsometry and their final porosity, and the corresponding thickness before and after sintering was obtained by BEMA and Cauchy fitting (Table 1). These results led to conclude that thickness increased with SDA concentration, also corresponding with a decrease of refractive index (and consequently an increase of porosity). However, the difference in final thickness (after sintering) of coatings prepared with 50 and 75 g/L of SDAs was only slight in comparison to the thickness difference observed between coatings prepared with 50 and 75 g/L of SDAs before sintering. Therefore, the material contraction of the coatings prepared with 75 g/L of SDA is higher than those prepared with 50 g/L of SDA.

Table 1

Refractive index (n) at 700 nm, apparent porosity, thickness of sintered coatings (d) and before sintering (d_{raw}) obtained from L-sols by spectral ellipsometry.

	n	Apparent porosity (%)	d (nm)	d_{raw}
L-SDA1-50g/L	1.34	25.6	95.3	192.9
L-SDA1-75g/L	1.24	45.7	111.3	371.7
L-SDA2-50g/L	1.39	14.0	76.9	151.8
L-SDA2-75g/L	1.38	16.1	78.5	244.5
L-SDA3-50g/L	1.31	31.7	178.3	252.8
L-SDA3-75g/L	1.22	50.3	278.5	417.2
L-SDA4-50g/L	1.24	44.4	102.4	188.0
L-SDA4-75g/L	1.28	36.6	104.0	311.6

The densification of the gel material during the thermal treatment is strongly dependent on its microstructure, and it is related to different mechanisms arising as temperature increases. The first event is the water loss, then inorganic network stabilization by further condensation of silica, and the decomposition of the organic phase [42]. Indeed, organic phase keeps a fixed volume during the sintering step, at least from ambient up to its decomposition temperature, that is around 200 ºC as can be observed in Table 2. Table 2 shows the temperatures at which a 5 % weight loss was detected by TGA, for each SDA. The experimental work revealed that the SDA1 and SDA3 started to decompose at ~ 180 ºC, followed by SDA4 at ~ 200 ºC while the cationic surfactant SDA2 started at ~ 220 ºC. TGA was further accomplished on sols prepared with and without SDA1 in order to observe the effect of the organic template. The resulting mass loss versus temperature curves are showed in Fig 6. In both cases a mass loss > 85 % was registered below 130 ºC, this fact being related to ethanol and water evaporation. After this point, the sol without SDA experimented a < 2 % mass loss in the 130 ºC – 350 ºC range, while the sol with SDA1 lost > 10 % of mass in this range. As can be observed for SDA1-sol, an inflection point appeared at < 200 ºC, related to the decomposition of the organic phase, also corresponding with the values analyzed in Table 2 for this SDA. Consequently, at temperatures below the decomposition temperature of organic phases (namely ~ T^a_5 in Table 2 for each SDA) the coating contraction is governed only by the volumetric contraction of the inorganic silica phase. However, at temperatures above the decomposition temperatures, the thickness decrease is related to the sum of the contraction of silica walls and the thermal decomposition of the organic phase. This thickness reduction is accompanied by a unidirectional contraction of the domain normal to the surface plane [40]. Finally, it can be pointed out that pores get empty through complete organic phase elimination. Depending on the

combination of polymer-like silica species such as linear, branched or cyclic and micelles created by the organic phase, the properties of the obtained mesoporous (pore size, wall thickness, specific area) shall be affected. The shrinkage after sintering coatings from sols with 50 g/L of SDA1, SDA2 or SDA4 was about 100 %, while coatings from sols with 75 g/L shrank 200 % after sintering. A higher quantity of SDA induced a higher thickness contraction during the thermal treatment and therefore it did not imply a proportional increase in porosity. A noteworthy effect was observed on the coatings derived from 50 g/L and 75 g/L SDA3, which only contracted 40 % and 50 %, respectively.

Table 2

Temperature at which each organic template lost 5 % mass (T^a_5) and 95 % mass(T^a_{95}) determined by TGA

	T^a_5 (ºC)	T^a_{95} (ºC)
SDA1	180	334
SDA2	217	440
SDA3	177	267
SDA4	203	320

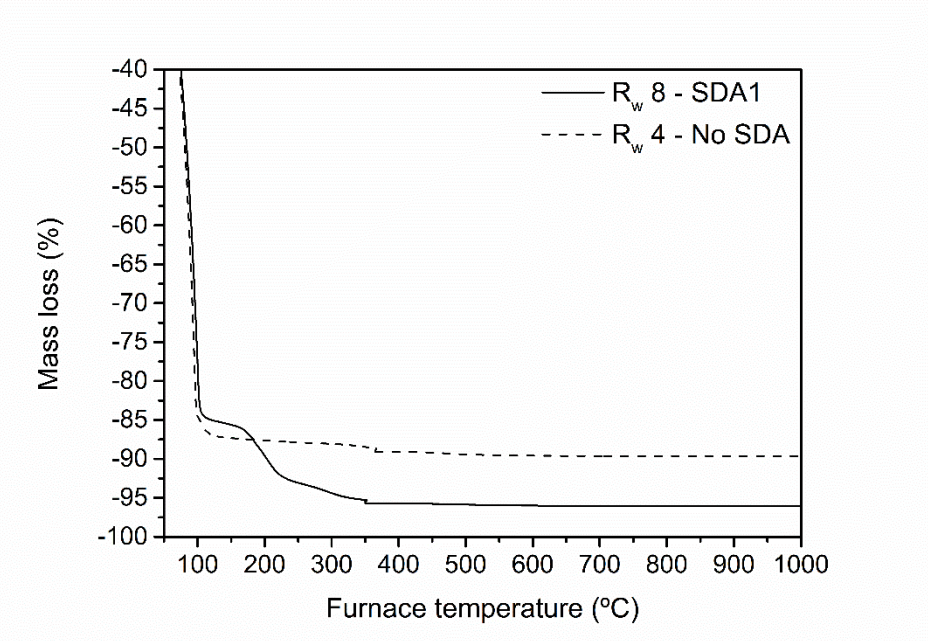

Fig. 6. Percentage of mass loss during TGA of sols with and without SDA1.

The increase in SDA3 and SDA1 concentration (from 50 to 75 g/L) provoked the largest effect on thickness and porosity of the coatings. Sols with increasing SDA3 concentration produced coatings with decreasing refractive index and increasing thickness values. SDA2-sols formed similar coatings in terms of thickness and porosity, while SDA4-sol with higher SDA quantity did not result in higher porosity in the formed coatings. In most cases, sols with R_w 8 led to coatings with lower refractive index and lower thickness when compared to sols with R_w 4 [8]. Therefore, higher R_w values during sol preparation allowed to achieve coatings with higher porosity and lower thickness. Water plays a relevant role in the hydrolysis and condensations steps. Excess water condensates within the sols contribute to their dilution and the growing of thinner coatings.

More balanced joint thickness-porosity values were achieved with L-sol containing 75g/L of SDA1, which made it the most suitable coating to achieve the higher transmittance values.

3.4.Optimized process and coating.

An ultimate optimization of the formulation was accomplished in which SDA1 and R_{Et} were accurately adjusted to 78 g/L concentration in order to deposit coatings with thickness between 120-130 nm and 50 % apparent porosity.

The viscosity of the sols prepared with R_w 8 and this optimized R_{Et}, with and without SDA1, was monitored up to one year and the results are depicted in Fig 7. It was revealed that sols with R_w 8 and the corresponding R_{Et} were very stable and independent of the presence of SDA1, which is very promising for the implementation and scaling up of the process.

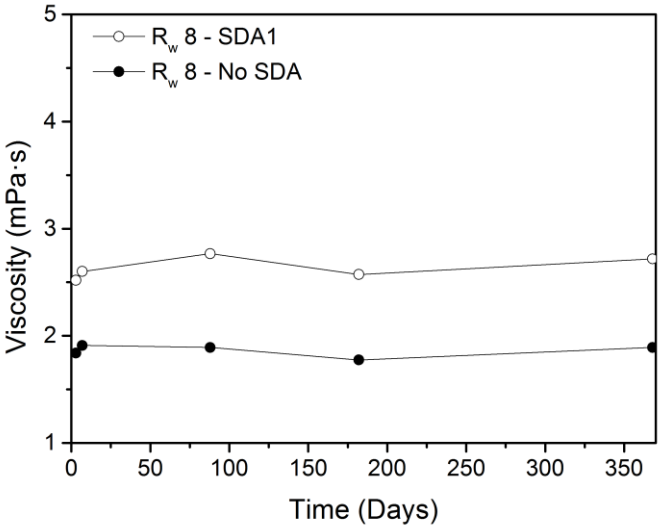

Fig. 7. Dynamic viscosity in the function of time for final sols prepared with and without SDA1. (Standard deviation < 0.05 mPa·s).

This sol formulation allowed to grow coatings with 50% porosity, refractive index 1.22 at 700 nm and 125 – 130 nm thick. The porosimetry of this type of coatings was analyzed by EEP, which provides the amount of adsorptive (water) inside pores from the variation of the optical characteristics of the coatings (thickness and refractive index), measured at several water partial pressures. Adsorption-desorption curves for coatings sintered at 350 ºC and 550 ºC and their respective pore size distribution are displayed in Figs. 8a and 8b, respectively. The coatings showed the typical behavior of mesoporous materials associated with type IV - V isotherms, according to IUPAC classification of adsorption isotherms of porous materials. The main difference between them was the related hysteresis loops, whose shape can be correlated to the texture (e.g., pore size distribution, pore geometry, and connectivity) of the mesoporous material [43]. The adsorption hysteresis of type IV - V isotherms is in turn classified by IUPAC in four types (H1 - H4) of curves. The studied coatings may be identified as H1 type, shaped by parallel branches and associated to well-defined cylindrical-like pore channels or agglomerates of approximately uniform spheres. The latter structure has

been observed and discussed in a previous work for this type of coatings [8]. Although the volume of pores was similar for coatings sintered at both temperatures, ~ 42 %, several differences were found between their isotherms. With the increasing of RH, little adsorption was observed up to capillary adsorption zone, which is characterized by a steep increase of adsorbed volume, detected at 55 % RH and 66 % RH for coatings sintered at 350 ºC and 550 ºC respectively. During capillary desorption, the decrease of the adsorbed water happened at RH around 53 % and around 58 % for coatings sintered at 350 ºC and 550 ºC, respectively. The effect of the capillary adsorption taking place at different RH values can be a consequence of different water-on-silica wetting angles. Differences among adsorption-desorption branches are associated to the difference in the radius of curvature of condensed liquid meniscus during the adsorption and desorption processes in the mesopores [31]. Water contact angle measurements confirmed the difference in the relative strength of fluid-wall for coatings sintered at two temperatures. Coatings sintered at 350 ºC showed 32.3 º ± 0.6 if prepared without SDA and 16.6 º ± 1.1 if prepared with SDA1. Coatings sintered at 550 ºC showed higher WCA, which can be related to the loss of free hydroxy groups being 48.8 º ± 1.4 on the coating prepared without SDA, while 19.5 º ± 1.4 was found for the coating with SDA1 content.

Pore size distribution was determined using modified Kelvin's equation [30] and the corresponding results are included in Fig. 8a and 8b. The coatings showed a narrow pore size distribution with maximum at 8 – 9 nm for both coatings.

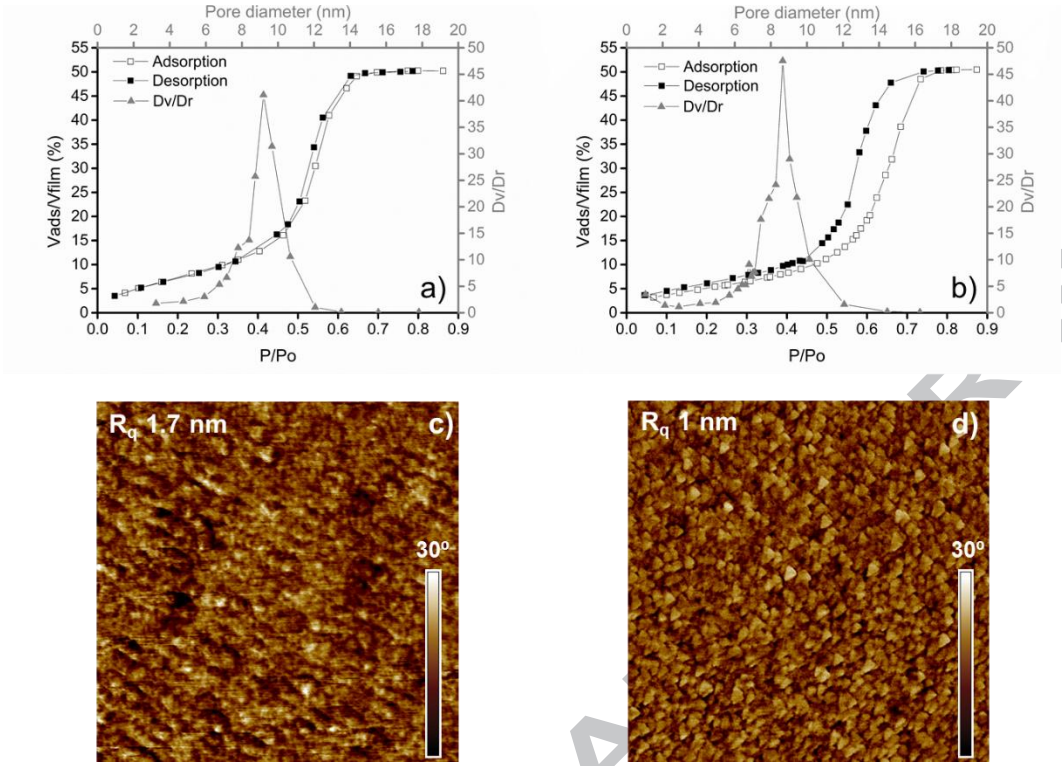

Fig. 8. Adsorption/desorption isotherm and pore size distribution of optimized coatings sintered at 350 ºC (a) and 550 ºC (b) and AFM phase images (1 µm x 1 µm) of the surface sintered at 350 ºC (c) and 550 ºC (d)

The porous structure of the coating was confirmed by AFM measurements, as showed in the surface images of coatings sintered at 350 ºC and 550 ºC in Figs. 8c and 8d, respectively. The surfaces of porous coatings sintered at two temperatures were homogeneous and did not present any crack. In both cases, the topography of the porous coatings was composed of small grains in which no particular order was detected. The size of these grains was 12 ± 3 nm for the coating sintered at 350 ºC and 7 ± 2 nm for the coating sintered at 550 ºC, which can be related to the high shrinkage due to the higher temperature. Moreover, these grains were comparable in size to the pore size obtained by EEP. Differences in the topography of coatings were observed since grains in the coating sintered at 550 ºC were packed closer and even connected to each other if compared with the coating sintered at 350 ºC. This result was also consistent with the

pore size obtained by EEP, which was somewhat smaller for the coating sintered at 550 ºC as can be observed by comparing Figs. 8a and 8b. Finally, the comparison between the image root mean square (RMS) roughness (R_q) of the coatings indicated that the surface of the coating sintered at 550 ºC was almost two times smoother than the surface of the coating sintered at 350 ºC.

Fig. 9 shows the transmittance and reflectance spectra of an AR mono-layer stack prepared from SDA1-containing sol and an AR bi-layer stack with inner coating obtained from no-SDA sol deposition and R_w 4, sequentially followed by outer coating deposition from SDA1-containing sol and R_w 8, which promoted the searched 50 % apparent porosity. Integrated transmittance in the 300 – 1500 nm cell operation range gave values of 96.5 % for the mono-layer and 96.8 % for the bi-layer stack. Thus, a 7.1 and 7.4 % increase over bare glass transmittance (90.1 %) was respectively achieved, while reflectance values were 2.2 % for the mono-layer and 2.0 % for the bi-layer stack.

The enhancement in the optical performance due to the developed AR coatings can be considered outstanding from the point of view of CPV applications and the results are even more promising considering the fact that the coating material was synthesized by acid-catalysis. As explained above, this is a process capable to settle coatings with robust mechanical properties and a very good adhesion. The bi-layer architecture was conceived with the aim to provide both a transmittance enhancement over a wider region of the solar spectrum and the capability to withstand harsh outdoor conditions (very common in the geographical regions where CPV modules are placed). The comparison with previously reported works is not as straightforward as might be expected, since most of them are focused on the design of porous mono-layers, and there is no uniformity in the studied wavelength ranges and the type of glass substrate. Coatings with similar refractive index were obtained by Liu et al. [44], who prepared

antireflective porous coatings by base-catalysis instead, and reported transmittance spectra only between 400-800 nm, similarly to other works that used an acid-catalyzed TEOS and cationic surfactant approach [45][26] and did not report either porosimetry or refractive index data. Therefore, no works based merely on acid-catalyzed TEOS and surfactant approach producing coatings with a thoroughly tailored porosity have been reported for this application. Among the works that have studied silica multi-layer stacks, several focused on stacks formed by an acid-catalyzed derived inner coating and a base-catalyzed external layer [20] [46]. Other works [47] developed two porous layers with different amounts of surfactant, however non comparable, narrower transmittance spectra and different properties to those found herein were reported.

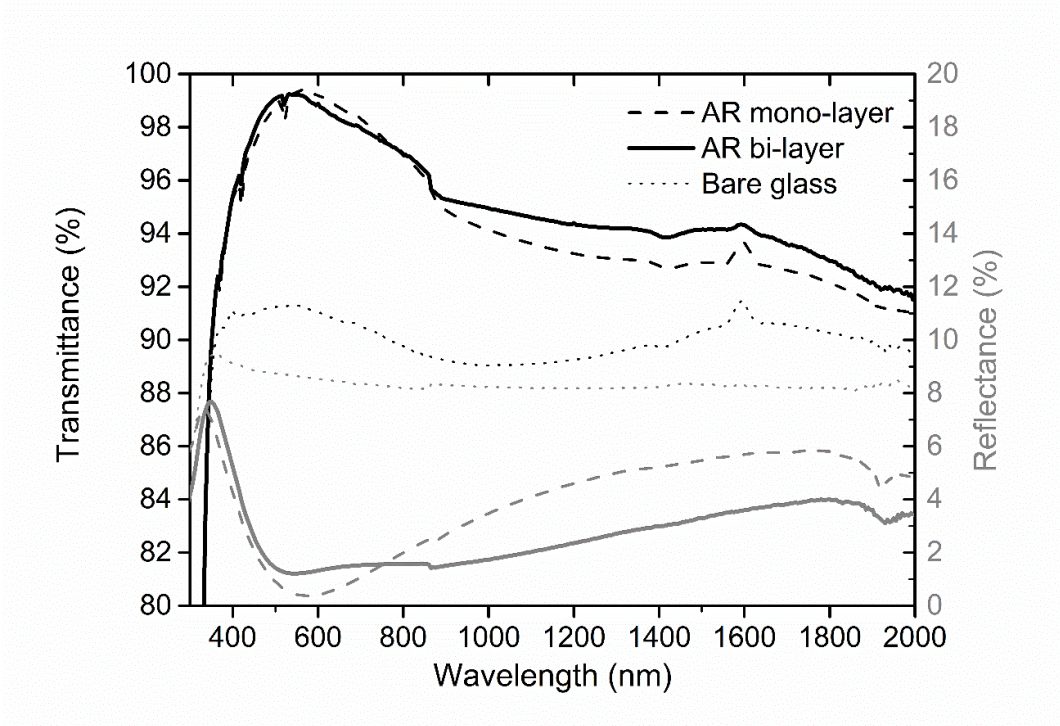

Fig. 9. Transmittance and reflectance spectra of mono- and bi-layer AR stacks.

Transmittance and reflectance spectra of optimized mono- and bi-layer AR stacks permitted to make calculations of their effect on the electrical production of a simplified module composed by a glass cover and a multijunction IMM3J cell. Short-circuit current density was calculated according to Equation 2 for the top, middle and bottom subcells of IMM3J cell and depicted in Fig. 10 for bare cell and cover glass + cell system, with and without mono- and bi-layer AR stacks. The current density of each subcell (bare cell) ranges between 13 and 14 mA/cm^2. Given that the subcells are connected in series, the one producing the lower current value limits the whole cell production [48]. In the system under study, it is the middle subcell which showed a lower current density. The presence of the indispensable cover glass interposed between the incoming photon flux source and cell, caused a drop in the photogenerated short-circuit current density of 8.7 % for the top, 9.9 % for middle and 10.3 % for bottom subcells, the system being still limited by the middle subcell. Mono- and bi-layer AR stacks coated on the glass substrate improved the photogeneration by 8 % on the top subcell. Middle subcell current was improved by 7.5 % by the mono-layer and 7.6 % by the bi-layer. The highest increase was observed for the bottom cell. In this particular case, in which middle subcell limits the photogeneration of the whole system, a slight enhancement was shown for the bi-layer AR stack. This case study demonstrates that, in order to provide a spectral performance consistent with the photogenerated current in the different subcells, AR coating stacks should ideally be designed to match the specific cell or module configurations targeted.

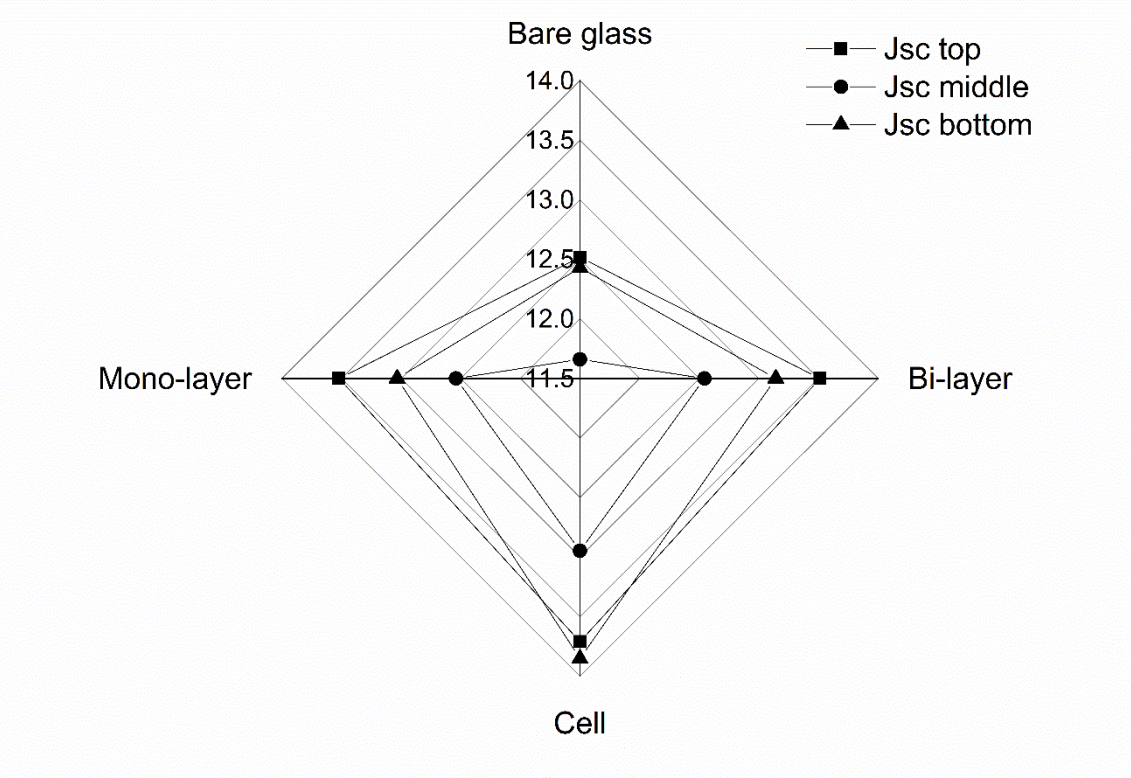

Fig. 10. Current density (mA/cm^2) calculated for each subcell in IMM3J without and with interposed bare or AR coated cover glass

4. Conclusions

An acid-catalyzed sol-gel approach has been tailored to experimentally develop two coatings integrating AR bi-layer or AR mono-layer stacks, showing broadband antireflection properties over the spectral response range of multijunction solar cells. The effect of the water content as a structure-regulating tool for the tailoring of the porosity of the external mono-layer has been studied in combination with four types of organic SDAs. R_w 8-sols have been proposed as candidates since it had been previously theoretically demonstrated that they lead to coating materials with a higher branched network. The theoretical approach was focused on providing higher porosity systems, with a structure close to those obtained by means of the basic-catalyzed approach but

simultaneously taking advantage of the properties attributed to the acid-catalyzed approach, such as robust mechanical properties to withstand harsh outdoor conditions. By means of NMR analysis, it was revealed that R_w 8-sols were formed by linear or ring-like and branched silica oligomers in an equilibrium state, and furthermore, it was evidenced that this equilibrium was not affected by the presence of organic micelles. In parallel, the viscosity evolution of sols with excess water, with and without SDA, has proven to be stable for at least one year. This fact contributes to providing a simple up-scaling and high efficiency process for implementation in CPV applications.

The suitability of the four types of organic SDAs as templates in R_w 8-sols was studied and a range of concentration values of organic and inorganic phases was scanned up in order to find the coating that best matched the joint thickness and porosity values.

Porosimetry and AFM measurements revealed that the sizes of the pore and the grain forming the coating were within the same order of magnitude. Therefore, mesoporous coatings with ~ 9 nm mean pore size, grain size between 7 - 12 nm and roughness R_q < 1.7 nm served to prepare the mono- and the bi-layer AR stacks, providing up to 7.4 % increase in transmittance over bare glass in the 300 to 1500 nm wavelength range. This enhanced transmittance spectra were used as inputs for the theoretical calculation of the short-circuit current density of a commercially available multijunction solar cell, showing a photogeneration enhancement over bare glass of 7.6 %, assigned to the limiting subcell.

This research has thus focused in the achievement of a stable and efficient process for AR coatings deposition targeting photovoltaic applications, based on the theoretical properties of acid-catalyzed sols with excess water. Although some works have been found in the literature based on similar acid-catalyzed approaches in combination with

SDAs, they have different aims and are not specifically and spectrally tailored for CPV applications. In this work, the optimization of several process and coating related properties such as sol aging and the mesostructure, together with the analysis and comparison of the optical properties of AR mono-layer and bi-layer stacks in a broadband region of solar spectrum constitutes an innovative approach. Since the composition and mesostructure were designed to provide robust mechanical properties and durability, the next step will be to analyze in detail the durability and the mechanical properties of the optimal candidates. The mono-layer and the bi-layer architecture will be compared in order to demonstrate whether the presence of the inner dense coating is capable to prevent alkali diffusion from the glass substrate to the external environment. Regarding the process itself, it will also be necessary to study the influence of the aging time of the sol on the processed coatings, and also to determine pot life according to the real operational conditions.

Acknowledgements

This work was supported by the Basque Government for EMAITEK 2017 program as well as the ELKARTEK projects FRONTIERS-2 (contract number KK2016-00093) and FRONTIERS-3 (contract number KK2017-00096).

The authors thank ICV-CSIC, Yolanda Castro and Alicia Durán for ellipsometry and EEP measurements.

The authors thank Miguel Pérez-Aradros for the help with graphical abstract illustration.

References

[1] M. Wiesenfarth, S.P. Philipps, A.W. Bett, K. Horowitz, S. Kurtz, Current status of concentrator photovoltaic (CPV) technology, U.S. Department of Energy Office of Scientific and Technical Information, 2017.

http://www.ntis.gov/help/ordermethods.aspx (accessed April 17, 2018).

[2] M.A. Green, K. Emery, Y. Hishikawa, W. Warta, E.D. Dunlop, Solar cell efficiency tables (version 47), Prog. Photovoltaics Res. Appl. 24 (2016) 3--11. doi:10.1002/pip.2728.

[3] S. Van Riesen, M. Neubauer, A. Boos, M.M. Rico, C. Gourdel, S. Wanka, R. Krause, P. Guernard, A. Gombert, New module design with 4-junction solar cells for high efficiencies, AIP Conf. Proc. 1679 (2015). doi:10.1063/1.4931553.

[4] The SunShot Initiative's 2030 Goal: 3¢ per Kilowatt Hour for Solar Electricity New Solar Opportunities for a New Decade, U.S. Department of Energy, 2016. https://www.energy.gov/sites/prod/files/2016/12/f34/SunShot 2030 Fact Sheet-12_16.pdf (accessed April 17, 2018).

[5] W. Cole, B. Frew, P. Gagnon, J. Richards, Y. Sun, J. Zuboy, M. Woodhouse, R. Margolis, SunShot 2030 for Photovoltaics (PV): Envisioning a Low-cost PV Future, U.S. Department of Energy, 2017. https://www.nrel.gov/docs/fy17osti/68105.pdf (accessed April 17, 2018).

[6] K. Burrows, V. Fthenakis, Glass needs for a growing photovoltaics industry, Sol. Energy Mater. Sol. Cells. 132 (2015) 455–459. doi:10.1016/j.solmat.2014.09.028.

[7] D. Chen, Anti-reflection (AR) coatings made by sol gel processes : A review, Sol. Energy Mater. Sol. Cells. 68 (2001) 313–336. doi:10.1016/S0927-0248(00)00365-2.

[8] C. Agustín-Sáenz, J.Á. Sánchez-García, M. Machado, O. Zubillaga, M. Brizuela, A. Tercjak, Broadband antireflective coating stack based on mesoporous silica by

acid-catalyzed sol-gel method for concentrated photovoltaic application, Sol. Energy Mater. Sol. Cells. 186 (2018) 154–164. doi:10.1016/j.solmat.2018.06.040.

[9] T. Asefa, M.J. MacLachlan, N. Coombs, G.A. Ozin, Periodic mesoporous organosilicas with organic groups inside the channel walls, Nature. 402 (1999) 867–871. doi:10.1038/47229.

[10] J.C. Brinker, Y. Lu, A. Sellinger, H. Fan, Evaporation-Induced Self-Assembly: Nanostructures Made Easy, Adv. Mater. 11 (1999) 579–585. doi:10.1002/(SICI)1521-4095(199905)11.

[11] J.C. Brinker, Hydrolysis and condensation of silicates: effects on structure, J. Non. Cryst. Solids. 100 (1988) 31–50.

[12] F. Orgaz-Orgaz, Gel to glass conversion: densification kinetics and controlling mechanisms, J. Non. Cryst. Solids. 100 (1988) 115–141.

[13] J.J. van Beek, D. Seykens, J.B.H. Jansen, R.D. Schuiling, Incipient polymerization of SiO2in acid-catalyzed TMOS sol-gel systems with molar water/alkoxide ratio between 0.5 and 32, J. Non. Cryst. Solids. 134 (1991) 14–22. doi:10.1016/0022-3093(91)90006-R.

[14] J.C. Pouxviel, J.P. Boilot, J.C. Beloeil, J.Y. Lallemand, NMR study of the sol/gel polymerization, J. Non. Cryst. Solids. 89 (1987) 345–360. doi:10.1016/S0022-3093(87)80277-6.

[15] W. Stober, A. Fink, Controlled Growth of Monodispersed Silica Spheres in the Micron Size Range, J. Colloid Interface Sci. 26 (1968) 62–69. doi:10.1016/0021-9797(68)90272-5.

[16] G. Engelhardt, W. Altenburg, D. Hoebbel, W. Wieker, 29Si- NMR- Spektroskopie an Silicatlösungen. IV. Untersuchungen zur Kondensation der Monokieselsäure, ZAAC - J. Inorg. Gen. Chem. 428 (1977) 43–52. doi:10.1002/zaac.19774280105.

[17] G. Engelhardt, Silicon-29 NMR of Solid Silicates, Encycl. Magn. Reson. (2007). doi:10.1002/9780470034590.emrstm0506.

[18] D. Collina, G. Fornasari, A. Rinaldo, F. Trifirò, G. Leofanti, G. Paparatto, G. Petrini, Silica preparation via sol-gel method: A comparison with ammoximation activity, Stud. Surf. Sci. Catal. 91 (1995) 401–410. doi:10.1016/S0167-2991(06)81776-3.

[19] X. Wang, J. Shen, Sol-gel derived durable antireflective coating for solar glass, J. Sol-Gel Sci. Technol. 53 (2010) 322–327. doi:10.1007/s10971-009-2095-y.

[20] X. Li, J. Shen, A scratch-resistant and hydrophobic broadband antireflective coating by sol-gel method, Thin Solid Films. 519 (2011) 6236–6240. doi:10.1016/j.tsf.2011.03.114.

[21] H. Ye, X. Zhang, Y. Zhang, L. Ye, B. Xiao, H. Lv, B. Jiang, Preparation of antireflective coatings with high transmittance and enhanced abrasion-resistance by a base/acid two-step catalyzed sol-gel process, Sol. Energy Mater. Sol. Cells. 95 (2011) 2347–2351. doi:10.1016/j.solmat.2011.04.004.

[22] G.S. Vicente, R. Bayón, A. Morales, Effect of Additives on the Durability and Properties of Antireflective Films for Solar Glass Covers, J. Sol. Energy Eng. 130 (2008) 011007. doi:10.1115/1.2804626.

[23] G. San Vicente, R. Bayón, N. Germán, A. Morales, Long-term durability of sol-

gel porous coatings for solar glass covers, Thin Solid Films. 517 (2009) 3157–3160. doi:10.1016/j.tsf.2008.11.079.

[24] M. Faustini, L. Nicole, C. Boissière, P. Innocenzi, C. Sanchez, D. Grosso, Hydrophobic, antireflective, self-cleaning, and antifogging sol-gel coatings: An example of multifunctional nanostructured materials for photovoltaic cells, Chem. Mater. 22 (2010) 4406–4413. doi:10.1021/cm100937e.

[25] D.B. Mahadik, R. V. Lakshmi, H.C. Barshilia, High performance single layer nano-porous antireflection coatings on glass by sol-gel process for solar energy applications, Sol. Energy Mater. Sol. Cells. 140 (2015) 61–68. doi:10.1016/j.solmat.2015.03.023.

[26] Y. Xu, C. Peng, C. Xin, J. Wu, Preparation of silica antireflective films for solar energy application, Mater. Lett. 94 (2013) 89–91. doi:10.1016/j.matlet.2012.12.013.

[27] R. Prado, G. Beobide, A. Marcaide, J. Goikoetxea, A. Aranzabe, Development of multifunctional sol-gel coatings: Anti-reflection coatings with enhanced self-cleaning capacity, Sol. Energy Mater. Sol. Cells. 94 (2010) 1081–1088. doi:10.1016/j.solmat.2010.02.031.

[28] A.L. Cauchy, Sur la réfraction et la réflexion de la lumière, Bull. Des Sci. Mathématiques. XIV (1830) 6–10.

[29] D.A.G. Bruggeman, Berechnung verschiedener physikalischer Konstanten von heterogenen Substanzen. I. Dielektrizitätskonstanten und Leitfähigkeiten der Mischkörper aus isotropen Substanzen, Ann. Der Phys. 24 (1935) 636–664. doi:10.1002/andp.19374210205.

[30] C. Boissière, D. Grosso, S. Lepoutre, L. Nicole, A.B. Bruneau, C. Sanchez, Porosity and Mechanical Properties of Mesoporous Thin Films Assessed by Environmental Ellipsometric, Langmuir. 21 (2005) 12362–12371.

[31] M.R. Baklanov, K.P. Mogilnikov, V.G. Polovinkin, F.N. Dultsev, Determination of pore size distribution in thin films by ellipsometric porosimetry, J. Vac. Sci. Technol. B. 18 (2000) 1385. doi:10.1116/1.591390.

[32] ASTM G173-03, Standard Tables for Reference Solar Spectral Irradiances: Direct Normal and Hemispherical on 37° Tilted Surface, 2013. doi:10.1520/G0173-03R12.2.

[33] M. Machado, T. Baenas, N. Yurrita, Optical model for multilayer glazing systems: Experimental validation through the analytical prediction of encapsulation-induced variation of PV modules efficiency, Sol. Energy. 135 (2016) 77–83. doi:10.1016/j.solener.2016.05.040.

[34] J. Boisvert, D. Law, R. King, E. Rehder, P. Chiu, D. Bhusari, C. Fetzer, X. Liu, W. Hong, S. Mesropian, R. Woo, K. Edmondson, H. Cotal, D. Krut, S. Singer, S. Wierman, N.H. Karam, High efficiency Inverted Metamorphic (IMM) solar cells, Conf. Rec. IEEE Photovolt. Spec. Conf. (2013) 2790–2792. doi:10.1109/PVSC.2013.6745051.

[35] D.C. Law, X.Q. Liu, J.C. Boisvert, E.M. Redher, C.M. Fetzer, S. Mesropian, R.R. King, K.M. Edmondson, B. Jun, R.L. Woo, D.D. Krut, P.T. Chiu, D.M. Bhusari, S.K. Sharma, N.H. Karam, Recent progress of Spectrolab high-efficiency space solar cells, Conf. Rec. IEEE Photovolt. Spec. Conf. (2012) 3146–3149. doi:10.1109/PVSC.2012.6318246.

[36] D.J. Friedman, Progress and challenges for next-generation high-efficiency multijunction solar cells, Curr. Opin. Solid State Mater. Sci. 14 (2010) 131–138. doi:10.1016/j.cossms.2010.07.001.

[37] J.F. Geisz, D.J. Friedman, J.S. Ward, A. Duda, W.J. Olavarria, T.E. Moriarty, J.T. Kiehl, M.J. Romero, A.G. Norman, K.M. Jones, 40.8% Efficient Inverted Triple-Junction Solar Cell With Two Independently Metamorphic Junctions, Appl. Phys. Lett. 93 (2008). doi:10.1063/1.2988497.

[38] W. Vogelsberger, A. Seidel, T. Breyer, Kinetics of sol particle formation as a function of pH studied by viscosity measurements in silica solutions, Langmuir. 18 (2002) 3027–3033. doi:10.1021/la0114878.

[39] K.W. Jang, S. Il Pyun, M.S. Jhon, The role of excess water in acidic sol-gel polymerization of tetraethoxysilane (TEOS) using molecular dynamics simulation, Mol. Simul. 29 (2003) 489–494. doi:10.1080/0892702031000103112.

[40] D. Grosso, F. Cagnol, G.J.D.A.A. Soler-Illia, E.L. Crepaldi, H. Amenitsch, A. Brunet-Bruneau, A. Bourgeois, C. Sanchez, Fundamentals of mesostructuring through evaporation-induced self-assembly, Adv. Funct. Mater. 14 (2004) 309–322. doi:10.1002/adfm.200305036.

[41] G.J.D.A.A. Soler-Illia, E.L. Crepaldi, D. Grosso, C. Sanchez, Block copolymer-templated mesoporous oxides, Curr. Opin. Colloid Interface Sci. 8 (2003) 109–126. doi:10.1016/S1359-0294.

[42] D. Kundu, H. Zhou, I. Honma, Thermally induced structural changes of lamellar and one-dimensional hexagonal mesoporous silica thin films, J. Mater. Sci. Lett.

17 (1998) 2089–2092.

[43] Z.A. Alothman, A review: Fundamental aspects of silicate mesoporous materials, Materials (Basel). 5 (2012) 2874–2902. doi:10.3390/ma5122874.

[44] B.T. Liu, W. De Yeh, Antireflective surface fabricated from colloidal silica nanoparticles, Colloids Surfaces A Physicochem. Eng. Asp. 356 (2010) 145–149. doi:10.1016/j.colsurfa.2010.01.003.

[45] X. Meng, Y. Wang, H. Wang, J. Zhong, R. Chen, Preparation of hydrophobic and abrasion-resistant silica antireflective coatings by using a cationic surfactant to regulate surface morphologies, Sol. Energy. 101 (2014) 283–290. doi:10.1016/j.solener.2013.12.038.

[46] Y. Zhang, F. Gao, L. Gao, L. Hou, Y. Jia, Study of tri-layer antireflection coatings prepared by sol – gel method, J. Sol-Gel Sci. Technol. 62 (2012) 134–139. doi:10.1007/s10971-012-2697-7.

[47] Y. Li, H. Lv, L. Ye, L. Yan, Y. Zhang, B. Xia, H. Yan, B. Jiang, Preparation of porous silica films in a binary template system for double-layer broadband antireflective coatings, RSC Adv. 5 (2015) 20365–20370. doi:10.1039/C4RA17141A.

[48] M. Victoria, C. Domínguez, I. Antón, G. Sala, Antireflective coatings for multijunction solar cells under wide-angle ray bundles, Opt. Express. 20 (2012) 8136–8147.